A New Structural BumpFoil Model With Application From Start-Up to FullOperating Conditions

Mihai Arghir, Omar Benchekroun

A New Structural Bump Foil Model With Application From Start-Up to Full Operating Conditions

Mihai Arghir & Omar Benchekroun

ISAE ENSMA, Institut PPRIME, UPR CNRS 3346, Université de Poitiers, Poitiers 86000, France

This paper presents a new structural bump foil model that can handle all operating con-ditions from start-up to full speed. The model is based on a nonlinear contact algorithm with friction and gaps. The top foil is modeled as a curved beam while bump foil uses a coupled truss model. The model considers the gaps between the bump foil and the bearing casing, between the bump foil and the top foil and between the rotor and the top foil. Thus, any numerical interference between the rotor and the top foil is avoided. A mixed lubrication model is used for the thin film pressures. Following this algorithm, contact pressures appear if the film thickness is less than three times the equivalent roughness of the rotor and of the top foil. Fluid pressures are calculated from numerical solutions of Reynolds equation while contact pressures, if present, are calculated with the model of Greenwood and Williamson. The model is validated by comparisons with the experimen-tal results obtained for start-up operating conditions of a first-generation foil bearing of 38.1 mm diameter with static loads of 10–50 N. Theoretical predictions of the start-up torque and takeoff speed compare well with experimental results. It is also shown how manufacturing bump height errors can explain the differences between theoretical and experimental predictions. Further validations are presented for the same bearing operat-ing at high speeds (30, 45, and 55 krpm) and heavy static loads (up to 200 N). The calcu-lated minimum film thickness and attitude angle are compared with experimental data from the literature.

Introduction

Aerodynamic foil bearings represent a technology that has proven advantages for supporting and guiding high-speed rotors of low and average power rotating machinery. One of the advantages is that they operate with a gas that can be either air or the process fluid. The power loss is then less than in ball bearings. The second advantage is that foil bearings, due to their compliant structure, may damp dynamic vibrations. This is an important point because the gas film has poor damping characteristics. The compliant foil structure is therefore one of the key points of this technology.

There are several types of foil bearing structures but the most widespread is the bump foil bearing made of a corrugated foil with bumps and a smooth top foil [1] (Fig. 1). The corrugated foil acts as a spring. The top foil collects the pressures in the thin gas film and transmits the load to the bumps. The relative displacements between the foils and the contact friction forces bring the desired damping.

Calculating the pressures in the thin gas film is not a difficult point, but modeling the foil structure has proved to be problematic. Indeed, the numerous published models distinguish themselves mainly through the model used for the compliant foil structure [2].

The first category of models uses a Winkler foundation description of the corrugated foil [3–8]. The interactions between bumps are neglected and the uniformly distributed stiffness of the foils is described by a simple formula. This category of models cannot predict energy dissipation; therefore, additional viscous damping [4] or structural loss [5] was added. These models are attractive because they are easy to implement and lead to quite rapid algorithms.

The top foil was discarded in the first models because it was correctly anticipated that it had a negligible stiffness compared to the corrugated foil. However, it was subsequently taken into account with finite elements [9–15] and it was shown how sagging between bumps may occur.

A second category of models went even further and discretized both the corrugated and top foils with structural finite elements, either as beams [16,17] or shells [18–20]. Interaction between bumps was naturally included. Coulomb friction was taken into account by using bookkeeping algorithms for the different stick-slip states of the contacts [16,17], or by using penalty [18,20] or Lagrange multipliers algorithms [19].

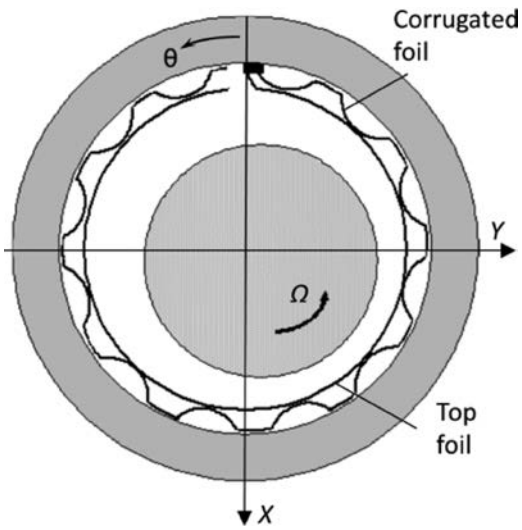

Fig. 1 The first-generation bump foil bearing

The next natural step was the use of nonlinear elasticity commercial codes for modeling the foils [21–24]. The results presented in Ref. [24] were the first to show the close-loose state of contacts during operation. The impact of the manufacturing errors of the compliant structure on the journal bearing characteristics was also underlined.

The structural model introduced in Ref. [25] can be situated between the first and second category of models. Each bump was modeled by a system of trusses. These trusses were assembled in a finite element like manner to obtain the stiffness matrix of the corrugated foil. The interaction between bumps was fully considered. The friction between the top and the bump foil was considered by using a regularized Coulomb law. However, the stiffness of the top foil was discarded. Similar structural models were next developed and some of them included the stiffness of the top foil [26–30].

Compared to the models of the second category, the model in Ref. [25] had the advantage of less computational effort. Therefore, it was recently extended for taking into account close-loose contacts between the foils, the bearing sleeve, and the rotor [31]. The top foil stiffness and an additional degree-of-freedom (DOF) per bump were added. Specific contact mechanics algorithms were employed [32]: the normal contact forces were calculated by using an augmented Lagrange multipliers (ALM) algorithm while a penalty method dealt with friction forces. The close-loose gap between the top foil and the rotor (i.e., the radial clearance of the bearing) was dealt with a penalty method and was a monolithic part of the solution. The new model and the employed numerical algorithms are detailed in Ref. [31]. Arghir and Benchekroun [31] present the results for the stiffness of the whole compliant structure obtained by pushing the rotor against the bearing. The influence of the bump height manufacturing errors and the interpretation given to the radial clearance of the bearing are also discussed in Ref. [31].[1]

This work presents the coupling of the new foil bearing structural model from Ref. [31] with the compressible air film. A mixed lubrication model is used for taking into account very small film thicknesses. Results are presented for both start-up and high speed/high static load operating conditions. The impact of bump height manufacturing errors on the start-up characteristics (start-up torque and lift-off speed) is also discussed. All the theoretical results compare well with experimental data from the literature [33,34], thus proving the capacity of the model to encompass all operating conditions.

The Foil Bearing Model

The bearing model is based on a structural model of the compliant foils and on the compressible thin film Reynolds equation adapted for taking into account the mixed lubrication regime.

The Structural Model of the Compliant Foils. The structural model of the compliant foils is depicted in Fig. 2 and it is the crucial part of the bearing model. The model is two-dimensional (2D) because it discards the variations of the elastic characteristics in the axial direction of the journal bearing.

Each bump has four DOF. For example, in Fig. 2, the DOF of the left bump are $u_{b,1}$, $u_{b,2}$, $u_{b,3}$, and $u_{b,4}$ and the DOF of the right bump are $u_{b,5}$, $u_{b,6}$, $u_{b,7}$, and $u_{b,8}$.

The top foil is discretized with nodes having only a transversal displacement. Each top foil node corresponds to a bump.

The model considers three gaps

- The gap between the top foil and the bump foil

$$g_{t,i} = g_{0_{t,i}} - u_{t,i} + u_{b,1+2(i-1)} \geq 0 \tag{1}$$

[1]Paper of Ref. [31] is available upon request.

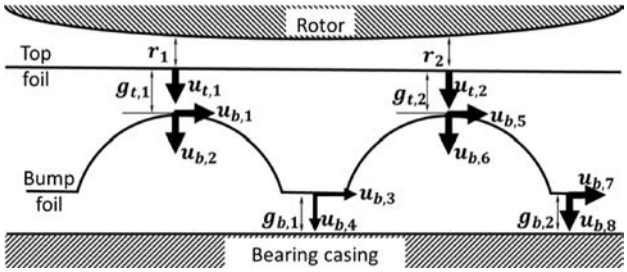

Fig. 2 The degrees-of-freedom and the gaps of the compliant structure

- The gap between the rotor and the top foil

$$g_{r,i} = r_i + u_{t,i} \geq 0 \tag{2}$$

- The gap between the bump foil and the sleeve

$$g_{b,i} = g_{0_{b,i}} - u_{b,2+2(i-1)} \geq 0 \tag{3}$$

where $r_i = C_r + x_r \cos\theta_i + y_r \sin\theta_i$, θ_i is measured in counter clockwise direction from the welding point (Fig. 1) and $i = 1 \ldots nb$.

The top foil is modeled as a curved beam with the plate correction. The corrugated foil is modeled by series of interacting springs that reproduce the coupled elastic behavior of the bumps. Both structural models are two-dimensional, i.e., the elasticity in the axial direction is not considered. The stiffness matrices of the top and bump foil were detailed in Ref. [31]. For clarity, they are also resumed in Appendices A and B.

The potential energy of the elastic foil structure is

$$\Pi = \frac{1}{2}\boldsymbol{u_b}^T \boldsymbol{K_b} \boldsymbol{u_b} + \frac{1}{2}\boldsymbol{u_t}^T \boldsymbol{K_t} \boldsymbol{u_t} \tag{4}$$

As indicated in Eqs. (1)–(3), the noninterference condition imposes non-negative values of the gap functions. If the gap functions (1)–(3) are positive, then the contacts are open, while if they are zero, then the contacts are closed. In this latter case, normal and tangential (friction) forces must be considered in the contacts. This is mathematically expressed by the Signorini–Moreau conditions [32]

$$g_i \geq 0,\ F_{n,i} \leq 0,\ g_i F_{n,i} = 0 \tag{5}$$

These constraints are included into the potential energy of the foil structure by using the augmented Lagrange multipliers method for the normal forces and the penalty method for the contacts between the rotor and the top foil and for the friction forces

$$\begin{aligned}\Pi_{\text{ALM}} = {} & \frac{1}{2}\boldsymbol{u_b}^T \boldsymbol{K_b} \boldsymbol{u_b} + \frac{1}{2}\boldsymbol{u_t}^T \boldsymbol{K_t} \boldsymbol{u_t} + \sum_{i=1}^{N_{\text{cntct}}} \left(\bar{\lambda}_i g_i + \frac{1}{2}\varepsilon_{\text{ALM}} g_i^2 \right) \\ & + \frac{1}{2}\sum_{i=1}^{N_{\text{Rotor}}} \varepsilon_r g_{r,i}^2 + \frac{1}{2}\sum_{i=1}^{N_{\text{stick}}} \varepsilon_f \left(u_{b,i} - u_{b,i}^{(0)} \right)^2 \\ & - \sum_{i=1}^{N_{\text{slip}}} \underbrace{f \bar{\lambda}_i \text{sign}(\dot{u}_{b,i})}_{F_{f,i}} \left(u_{b,i} - u_{b,i}^{(0)} \right)\end{aligned} \tag{6}$$

The augmented Lagrange multiplier $\bar{\lambda}_i$ is iteratively updated following Uzawa algorithm [32]

$$\bar{\lambda}_i^{(n+1)} = \bar{\lambda}_i^{(n)} + \varepsilon_{\text{ALM}} g_i^{(n+1)} \tag{7}$$

The equations obtained by minimizing the potential energy yield

$$\begin{bmatrix} [\boldsymbol{K_b}+\boldsymbol{L_{bb}}]_{4nb,4nb} & [\boldsymbol{L_{bt}}]_{4nb,nb} \\ [\boldsymbol{L_{tb}}]_{nb,4nb} & [\boldsymbol{K_{t11}}+\boldsymbol{L_{tt}}]_{nb,nb} \end{bmatrix} \begin{Bmatrix} \{\boldsymbol{u_b}\}_{4nb} \\ \{\boldsymbol{u_{t1}}\}_{nb} \end{Bmatrix} = \begin{Bmatrix} \{\boldsymbol{F_b}\}_{4nb} \\ \{\boldsymbol{F_{t1}}\}_{nb} \end{Bmatrix} \tag{8}$$

alternatively, with notations that are more compact

$$\boldsymbol{K_{bt1}}\boldsymbol{u_{bt1}} = \begin{Bmatrix} \boldsymbol{F_b} \\ \boldsymbol{F_{t1}} \end{Bmatrix} \tag{9}$$

$$\boldsymbol{K_{bt1}} = \begin{bmatrix} \boldsymbol{K_b}+\boldsymbol{L_{bb}} & \boldsymbol{L_{bt}} \\ \boldsymbol{L_{tb}} & \boldsymbol{K_{t11}}+\boldsymbol{L_{tt}} \end{bmatrix} \tag{10}$$

$$\boldsymbol{u_{bt1}} = \begin{Bmatrix} \boldsymbol{u_b} \\ \boldsymbol{u_{t1}} \end{Bmatrix} \tag{11}$$

where the coupling matrices $\boldsymbol{L_{bb}}$, $\boldsymbol{L_{tb}} = \boldsymbol{L_{bt}^T}$, $\boldsymbol{L_{tt}}$ and the vectors $\boldsymbol{F_b}$, $\boldsymbol{F_{t1}}$ contain the penalties and the Lagrange multipliers needed for dealing with contacts. For example, for a corrugated foil with only one bump, these matrices and vectors write

$$\begin{aligned} \boldsymbol{L_{bb}} &= \mathrm{DIAG}\begin{Bmatrix} \varepsilon_f \mathrm{ISTICK}_t \\ \varepsilon_{ALM} \\ \varepsilon_f \mathrm{ISTICK}_b \\ \varepsilon_{\mathrm{ALM}} \end{Bmatrix} \\ \boldsymbol{L_{bt}} &= \begin{bmatrix} 0 \\ -\varepsilon_{\mathrm{ALM}} \\ 0 \\ 0 \end{bmatrix} = \boldsymbol{L_{tb}^T} \\ L_{tt} &= \varepsilon_{\mathrm{ALM}} + \varepsilon_r \\ \boldsymbol{F_b} &= \begin{Bmatrix} \varepsilon_f u_{b,1}^{(0)} \mathrm{ISTICK}_t + f\bar{\lambda}_t \mathrm{sign}(\dot{u}_{b,1})(\mathrm{ISTICK}_t - 1) \\ -\bar{\lambda}_t - \varepsilon_{\mathrm{ALM}} g_{0_t} \\ \varepsilon_f u_{b,3}^{(0)} \mathrm{ISTICK}_b + f\bar{\lambda}_b \mathrm{sign}(\dot{u}_{b,3})(\mathrm{ISTICK}_b - 1) \\ \bar{\lambda}_b + \varepsilon_{\mathrm{ALM}} g_{0_b} \end{Bmatrix} \\ F_{t1} &= \bar{\lambda}_t + \varepsilon_{\mathrm{ALM}} g_{0_t} - \varepsilon_r r \end{aligned} \tag{12}$$

The system of Eq. (9) is nonlinear because $\boldsymbol{F_b}$ and $\boldsymbol{F_{t1}}$ contain the friction forces. The system is solved by using a Newton–Raphson algorithm that was given in Ref. [31]. A regularized Coulomb friction law is used for stabilizing this algorithm.

Finally, the global contact algorithm consists of three embedded loops and its flow chart is depicted in Fig. 3.

The Thin Film Flow Model for Mixed Lubrication. The thin film flow is governed by Reynolds equation for a compressible fluid. For an isothermal flow regime, this writes

```
Initialize contacts
DO i=1, nb
    IF(g_t<0) THEN the contact is closed
    ELSE the contact is loose
END DO
DO WHILE contact states are not converged
    DO WHILE normal contact forces are not converged
        DO WHILE friction forces are not converged
            Solve eq. (9) by using a Newton algorithm
        END DO ! friction forces
    END DO ! normal contact forces
    Check changes of contact states
END DO ! contact states do not change = convergence
```

Fig. 3 Pseudocode of the contact algorithm

$$\frac{\partial}{\partial x}\left(\frac{\tilde{P}h^3}{12\mu}\frac{\partial P}{\partial x}\right) + \frac{\partial}{\partial z}\left(\frac{\tilde{P}h^3}{12\mu}\frac{\partial P}{\partial z}\right) = \frac{R\Omega}{2}\frac{\partial(\tilde{P}h)}{\partial x} + \frac{\partial(\tilde{P}h)}{\partial t} \tag{13}$$

where $x = R\theta$. The boundary conditions are

$$P = P_{\mathrm{ext}} \text{ at } \theta = 0,\ z = 0, \text{ and } z = L \tag{14}$$

The Reynolds equations are discretized by using the finite volume method on a rectangular mesh with equally spaced grids [35]. The resulting discretized equations are nonlinear due to the presence of $\tilde{P}$ on left-hand side of Eq. (13). The system is then solved by using the Newton–Raphson method. The numerical solution is stabilized by "upwinding" the $\tilde{P}$ pressures in Eq. (13).

Solving only Eq. (13) supposes that full lubrication conditions are met in the thin film flow. This is the case if $h/\sigma_{\mathrm{eq}} \geq 7$, where $\sigma_{\mathrm{eq}} = \sqrt{\sigma_R^2 + \sigma_t^2}$ is the combined standard deviation of the rotor and of the top foil roughness.

However, the film thickness in foil bearings can be very low and contacts between asperities may arise. In this case, the bearing operates under local mixed lubrication regime. This is true when $1 \leq \bar{h}_{\mathrm{eq}} \leq 3$ and contact pressures must be added to the fluid film pressures calculated by solving Eq. (13).

Two other operating conditions must also be underlined.

- If $\bar{h}_{eq} \leq 1$, then the contact pressure between the asperities is large and the dissipated energy is very high. Operating conditions under this regime will rapidly damage the foil bearing because the foil structure cannot efficiently evacuate the generated heat.
- If $3 \leq \bar{h}_{\mathrm{eq}} \leq 7$, there are no contacts between the roughness asperities. Nevertheless, the height of the thin film must consider the roughness profile of the two surfaces. This may be done by correcting the Reynolds equation (13) with flow factors [36].

The contact pressures were deduced by using the model of Greenwood and Williamson [37] given in Appendix C. Contact pressures are calculated in every discretization cell of the Reynolds equation where the condition $1 \leq \bar{h}_{\mathrm{eq}} \leq 3$ holds

$$P_{\mathrm{cntct}} = \frac{4}{3}(\eta_R + \eta_t)E_{\mathrm{eq}}\sqrt{\beta}\int_h^\infty (y_s - h)^{3/2}\mathcal{F}(y_s)dy_s \tag{15}$$

Fluid and contact pressures are integrated over the rotor and the top foil surface. For the rotor, this yields

$$\begin{aligned} F_X = &\int_0^{2\pi}\int_0^L (P - P_{\mathrm{ext}} + P_{\mathrm{cntct}})\cos\theta R d\theta dz \\ &- f\int_0^{2\pi}\int_0^L P_{\mathrm{cntct}}\sin\theta R d\theta dz \end{aligned} \tag{16}$$

$$\begin{aligned} F_Y = &-\int_0^{2\pi}\int_0^L (P - P_{\mathrm{ext}} + P_{\mathrm{cntct}})\sin\theta R d\theta dz \\ &+ f\int_0^{2\pi}\int_0^L P_{\mathrm{cntct}}\cos\theta R d\theta dz \end{aligned} \tag{17}$$

For the top foil, the pressures are averaged over the bearing length because the structural model is two-dimensional

$$P_{\mathrm{avrg}} = \frac{1}{L}\int_0^L (P + P_{\mathrm{cntct}})dz \tag{18}$$

The radial force applied on the top foil is

$$F_{Pi} = \left(P_{\mathrm{avrg}} - P_{\mathrm{ext}}\right)R\left(\theta_{i+1/2} - \theta_{i-1/2}\right)L \tag{19}$$

The torque on the rotor and on the top foil can also be calculated

$$C_{z,R/t} = \int_0^{2\pi}\int_0^{L} \left(\tau_{x,R/t} + fP_{\text{cntct}}\right) R d\theta dz \tag{20}$$

where $\tau_{x,R/t}$ is the rotor/top foil shear stress in the circumferential direction [38].

The two-dimensional structural model with the axially averaged pressure is the strongest simplifying assumption used in the present approach. It will be underlined further in this paper the impact that it has on the results.

Coupling the Structural Model With Reynolds Equation. In the previous work [31], the discretization nodes of the top foil coincided with the bumps. This discretization was sufficient for simple loading cases, when the rotor was pushed into the stator. However, the numerical solution of the Reynolds equation requires a finer mesh in the circumferential direction. For example, if a foil journal bearings has between $nb = 20\ldots30$ bumps, the number of discretization points in the circumferential direction for the Reynolds equation, nx, is at least the double. In the same time, the contact algorithm requires a stiffness matrix of the top foil with a clear distinction between points where contact may occur (i.e., the top of the bumps) and the rest. A stiffness matrix for the top foil is then generated by using Eq. (B1) and for the points corresponding to the bumps, nb, and to the discretization points of the Reynolds equation, nx. The calculation of the stiffness matrix requires the discretization nodes organized with increasing circumferential coordinate starting from the welding (Fig. 1) in clockwise direction. The stiffness matrix of the top foil, $\boldsymbol{K_t}$, will be square and of dimension $nb + nx$. The matrix is then reorganized by making distinction between the DOF of the top foil associated with the bumps, $u_{t1,i=1\ldots nb}$, were contacts may occur and the DOF associated with the discretization nodes of the Reynolds equation, $u_{t2,i=1\ldots nx}$

$$[K_t]_{nb+nx,nb+nx} = \begin{bmatrix} [K_{t,11}]_{nb,nb} & [K_{t,12}]_{nb,nx} \\ [K_{t,21}]_{nx,nb} & [K_{t,22}]_{nx,nx} \end{bmatrix} \tag{21}$$

The total potential energy of the structure with gaps and contacts given by Eq. (6) must also include the degrees of the freedom of the top foil introduced by the Reynolds equation discretization nodes, $\boldsymbol{u_{t2}}$ and the mechanical work of the pressure forces $\boldsymbol{F_{p1}}$ and $\boldsymbol{F_{p2}}$ acting on the top foil. The nonlinear system of equations obtained by minimizing the total potential energy of the structure with contacts and friction writes

$$\begin{bmatrix} [K_b + L_{bb}]_{4nb,4nb} & [L_{bt}]_{4nb,nb} & [0]_{4nb,nx} \\ [L_{tb}]_{nb,4nb} & [K_{t11} + L_{tt}]_{nb,nb} & [K_{t12}]_{nb,nx} \\ [0]_{nx,4nb} & [K_{t21}]_{nx,nb} & [K_{f22}]_{nx,nx} \end{bmatrix} \begin{Bmatrix} \{u_b\}_{4nb} \\ \{u_{t1}\}_{nb} \\ \{u_{t2}\}_{nx} \end{Bmatrix} = \begin{Bmatrix} \{F_b\}_{4nb} \\ \{F_{t1} + F_{p1}\}_{nb} \\ \{F_{p2}\}_{nx} \end{Bmatrix} \tag{22}$$

moreover, with notations that are more compact

$$\begin{bmatrix} \boldsymbol{K_{bt1}} & \boldsymbol{L_{t12}} \\ \boldsymbol{L_{t21}} & \boldsymbol{K_{t22}} \end{bmatrix} \begin{Bmatrix} \boldsymbol{u_{bt1}} \\ \boldsymbol{u_{t2}} \end{Bmatrix} = \begin{Bmatrix} \boldsymbol{F_{bt1}} \\ \boldsymbol{F_{p2}} \end{Bmatrix} \tag{23}$$

$$\boldsymbol{L_{t21}} = \begin{bmatrix} \boldsymbol{0} & \boldsymbol{K_{t21}} \end{bmatrix} = \boldsymbol{L_{t12}}^{\boldsymbol{T}}, \quad \boldsymbol{K_{t12}} = \boldsymbol{K_{t21}}^{\boldsymbol{T}} \tag{24}$$

$$\boldsymbol{F_{bt1}} = \begin{Bmatrix} \boldsymbol{F_b} \\ \boldsymbol{F_{t1}} + \boldsymbol{F_{p1}} \end{Bmatrix} \tag{25}$$

The vector $\boldsymbol{u_{bt1}}$ contains all the displacements of the bumps and the displacements of the top foil related to bumps. The vector $\boldsymbol{u_{t2}}$ contains the displacements of the top foil corresponding to the discretization nodes of the Reynolds equation. Both vectors are deduced by solving the system of Eq. (23)

```
Initialize film thickness
IF(h<0) Solve contacts
DO WHILE (error_h ≤ precision)
    Calculate fluid pressures ! solve eq. (13) and (14)
    IF(h ≤ 3σ_eq) Calculate contact pressures ! eq. (15)
    Calculate foil displacements ! eq. (26), Figure 3, eq. (27)
    Calculate film thickness ! eq. (28), (29)
END DO
```

Fig. 4 Pseudocode of the global foil bearing algorithm

$$\left(\boldsymbol{K_{bt1}} - \boldsymbol{L_{t12}}\boldsymbol{K_{t22}}^{-1}\boldsymbol{L_{t21}}\right)\boldsymbol{u_{bt1}} = \boldsymbol{F_{bt1}} - \boldsymbol{L_{t12}}\boldsymbol{K_{t22}}^{-1}\boldsymbol{F_{p2}} \tag{26}$$

$$\boldsymbol{u_{t2}} = \boldsymbol{K_{t22}}^{-1}\left(\boldsymbol{F_{p2}} - \boldsymbol{L_{t21}}\boldsymbol{u_{bt1}}\right) \tag{27}$$

The system of Eq. (26) for calculating $\boldsymbol{u_{bt1}}$ is nonlinear because $\boldsymbol{F_b}$ and $\boldsymbol{F_{t1}}$ in $\boldsymbol{F_{bt1}}$ contain the friction forces. The solution algorithm is identic to the one used in Ref. [31] for solving Eq. (9) and depicted in Fig. 3. This is possible because the terms introduced in Eq. (26) by considering the DOFs of the top foil in the discretization nodes of the Reynolds equation, $\boldsymbol{L_{t12}}\boldsymbol{K_{t22}}^{-1}\boldsymbol{L_{t21}}$ and $\boldsymbol{L_{t12}}\boldsymbol{K_{f22}}^{-1}\boldsymbol{F_{p2}}$ are constant, linear terms.

The displacements of the top foil in the discretization nodes of the Reynolds equation are then obtained by simply solving the linear system (27). They are then added to the gas film thickness

$$h = r + u_t = C_r + x_r\cos\theta + y_r\sin\theta + u_t \tag{28}$$

that is exactly the gap function (2). The contact algorithm thus ensures that the rotor and the top foil cannot interfere.

The calculation of the film thickness follows an iterative procedure with under-relaxation

$$h^{(n+1)} = h^{(n)} + \mathfrak{r}_{h\text{film}}\left(h^{(*)} - h^{(n)}\right) \tag{29}$$

where $h^{(*)}$ is the film thickness given by Eq. (28). The whole algorithm is described in Fig. 4.

Results

Two kinds of results are presented for depicting the predictive capacity of the model: start-up and full operating conditions under a heavy steady load. The geometry of the first-generation foil bearing used in all calculations is given in Fig. 1, Table 1, and Fig. 5.

Start-Up Analysis. The start-up is modeled as a succession of steady operating conditions with given rotation speed and steady load. Acceleration effects are neglected. The calculations are performed for rotation speeds starting from 10 rpm, i.e., very close to zero. In this case, the rotor is in contact with the top foil and mixed lubrication conditions prevail over the entire contact zone. The velocity is gradually increased and the extent of the mixed lubrication zone will decrease while the compressible gas film starts to separate the rotor from the top foil. This situation is depicted in Figs. 6 and 7.

Table 1 Foil bearing characteristics

Bearing axial length, L	38.1 mm	Young modulus, E	214 GPa
Rotor radius, R	19.05 mm	Poisson coefficient, ν	0.29
Radial clearance, C_r	31.8 μm	Bump pitch, p_b	4.572 mm
No. of bumps, n_b	26	Bump width, $2l_0$	3.556 mm
Foil thickness, $e_b = e_t$	0.102 mm	Bump height, h_b	0.508 mm

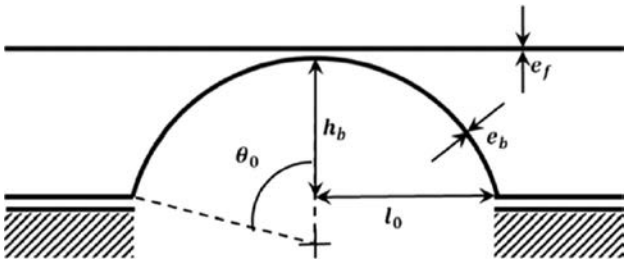

Fig. 5 Geometry of the bump

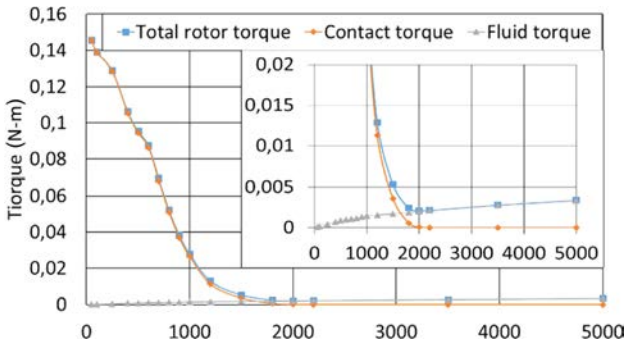

Fig. 6 Rotor torque versus rotation speed during start-up ($W_x = 30$ N, $C_r = 31.8\,\mu$m, $f = 0.25$)

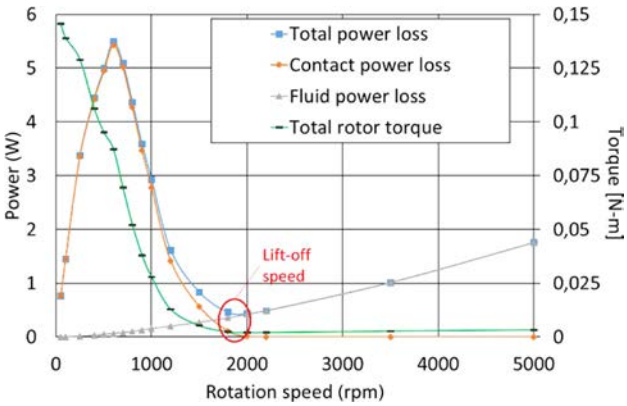

Fig. 7 Power and torque versus speed during start-up ($W_x = 30$ N, $C_r = 31.8\,\mu$m, $f = 0.25$)

Figure 6 depicts the rotor torque versus the rotational speed for a static load $W_x = 30$ N ($W_y = 0$) and a radial clearance of 31.8 μm. Three values of the torque are depicted: the torque due to the contact between the asperities of the rotor and the top foil surface, the fluid torque and the total torque. The contact torque is rapidly decreasing with the rotation speed and becomes zero when a full gas film supports the rotor. The fluid torque increases very slowly with the rotation speed and the total torque inherits the characteristics of both the contact and the fluid torque. The maximum value of the total torque is the start-up (or break-away) torque. Its value is entirely due the contact forces. The speed when the contact torque vanishes is the lift-off (or start-up) speed.

Figure 7 depicts the power loss, i.e., the torque in Fig. 6 multiplied by the rotation speed. The lift-off speed corresponds to the minimum of the power loss variation versus the rotation speed. It can be seen that, exactly as in measurements, the variations of the power loss enable a more accurate reading of the lift-off speed than the torque variation.

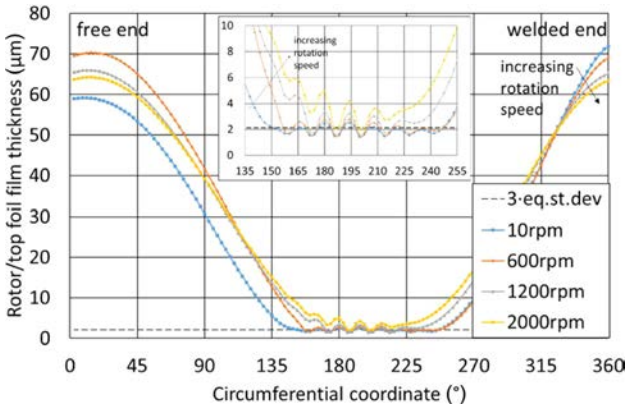

Fig. 8 Rotor/top foil film thickness circumferential variation ($W_x = 30$ N, $C_r = 31.8\,\mu$m, $f = 0.25$)

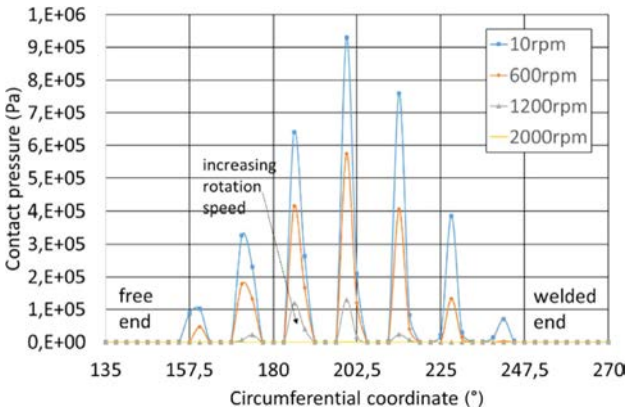

Fig. 9 Contact pressure circumferential variation ($W_x = 30$ N, $C_r = 31.8\,\mu$m, $f = 0.25$)

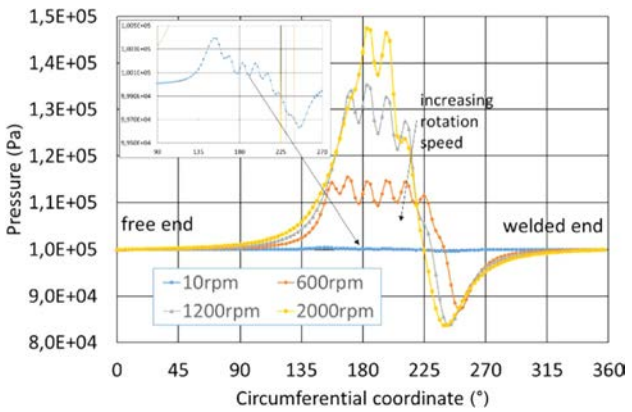

Fig. 10 Fluid pressure circumferential variation ($W_x = 30$ N, $C_r = 31.8\,\mu$m, $f = 0.25$)

The circumferential variations of the rotor/top foil film thickness, of the contact pressure, and of the fluid pressure for a static load of 30 N are depicted from Figs. 8 to 10. The sagging of the top foil between bumps and its effects on the contact and on the fluid pressure are clearly visible. The upper limit of the mixed lubrication regime, i.e., $h = 3\sigma_{eq}$, is depicted with a dotted line in Fig. 8. The $\Omega = 2000$ rpm lift-off speed of the case depicted in Figs. 8–10 corresponds to the limit when $h \geq 3\sigma_{eq}$ and all contact pressures are zero.

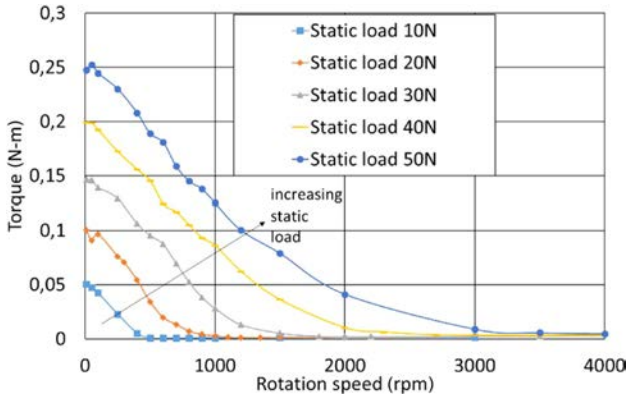

Fig. 11 Contact torque versus speed during start-up for different static loads ($C_r = 31.8\ \mu$m, $f = 0.25$)

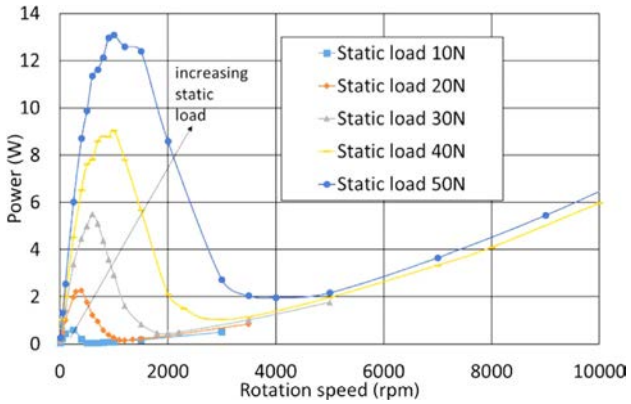

Fig. 12 Total power loss versus speed during start-up for different static loads ($C_r = 31.8\ \mu$m, $f = 0.25$)

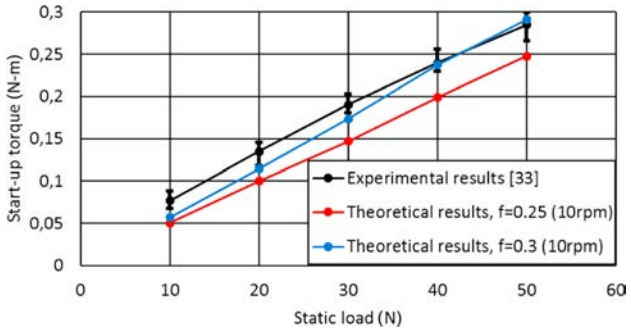

Fig. 13 Start-up torque versus static load ($C_r = 31.8\ \mu$m)

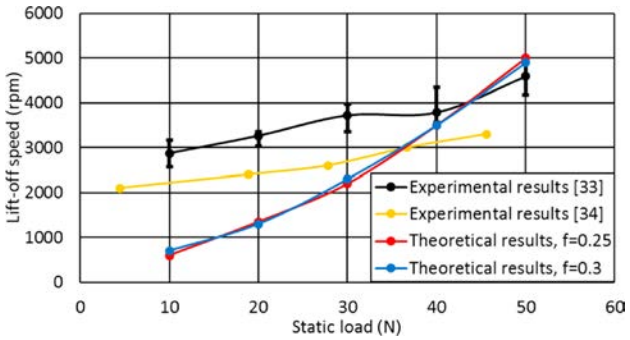

Fig. 14 Lift-off speed versus static load ($C_r = 31.8\ \mu$m)

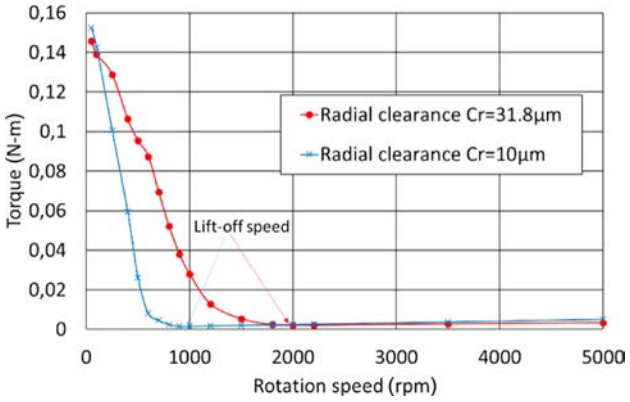

Fig. 15 Total torque versus rotation speed for $C_r = 31.8\ \mu$m and 10 μm ($W_x = 30$ N, $f = 0.25$)

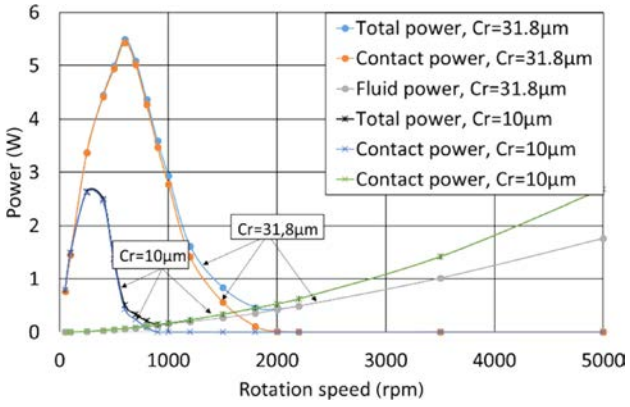

Fig. 16 Power loss versus rotation speed for $C_r = 31.8\ \mu$m and 10 μm ($W_x = 30$ N, $f = 0.25$)

Figures 11 and 12 depict the contact torque and the total power loss during start-up for different static loads. As expected, the start-up torque and the lift-off velocity increase with the static load.

In Fig. 13, the calculated start-up torque is compared to the measurements from Ref. [33]. Friction coefficients $f = 0.25$ and 0.3 were used in calculations. It can be seen that calculations follow exactly the measured curved and the values obtained with a friction coefficient $f = 0.3$ are very close to experiments.

Figure 14 depicts the comparison between the theoretical lift-off speed calculated with $C_r = 31.8\ \mu$m and values measured in Ref. [33]. The results of measurements made by Ruscitto et al. in Ref. [34] for the same bearing are also presented. The theoretical values are lower and increase more rapidly with the static load than measurements. The friction coefficient used in calculations (0.25 and 0.3) has no impact on the lift-off speed.

Any theoretical model can be suspected of inaccuracies but the discrepancies shown in Fig. 14 may also indicate that the geometrical characteristics of the foil bearings tested in Ref. [33] were not exactly the ones given in Table 1. It is known that the radial clearance of the foil bearing is a parameter that is difficult to measure. Ruscitto et al. [34] proposed a method based on static loading tests that were further made popular by Rubio and San Andrés [5]. The method is based on the interpretation of static load/displacement curve and is systematically used because, up to now, it is the only reliable way of experimentally estimating the radial clearance. However, the values reported in the literature for the foil bearing described in Table 1 may be quite different.

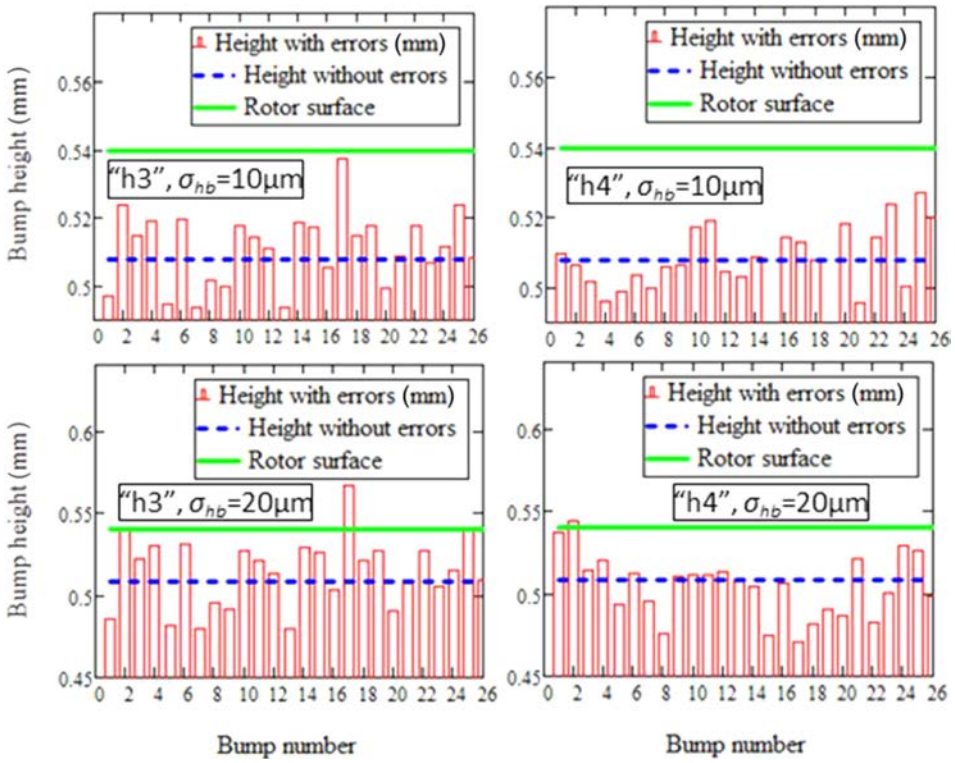

Fig. 17 Bump height distribution errors ($C_r = 31.8\ \mu$m)

Calculations where then made with a value of 10 μm of the radial clearance.

Figure 15 shows the comparison between the torques calculated with radial clearances of 31.8 μm and 10 μm. The value of the start-up torque increased very slightly when the radial clearance decreased from 31.8 μm to 10 μm but the lift-off speed was almost divided by two. This result shows that a small radial clearance favors the pressure generation in the thin film (the "oil wedge" effect) and therefore the creation of lift with increasing rotation speed. In the meantime, the radial clearance is of less importance for the start-up torque because this latter parameter depends on the static load, on the stiffness of the compliant foil structure and on the rotor/top foil friction coefficient.

Figure 16 depicts the comparisons between the power losses calculated with radial clearances of 31.8 μm and 10 μm. The bearing with $C_r = 10\ \mu$m necessitates a lower power for start-up, but operates with a slightly larger power loss after lift-off.

Impact of Bump Height Manufacturing Errors. The compliant structure of foil bearing is always affected by manufacturing errors. It is, however, not realistic to replace the design value of the radial clearance by another constant for considering these errors. The authors showed in Ref. [24] that manufacturing errors of the height of the bump foil lead to a circumferential variation of the radial clearances that is different from the theoretical constant value. Six different random bump height distributions were analyzed in Ref. [24]. Among them, the case designed as "h3" had the highest static foil stiffness and the case "h4" had the lowest static foil stiffness.[2] These two cases are now analyzed for start-up conditions.

Their bump height distributions are depicted in Fig. 17 for two values of the standard deviation, $\sigma_{hb} = 10\ \mu$m and $\sigma_{hb} = 20\ \mu$m (the average value of the bump height is the design value, $h_b = 508\ \mu$m).

[2]Other bump height error distributions than the six cases analyzed in Ref. [24] may show lower or higher static foil stiffness.

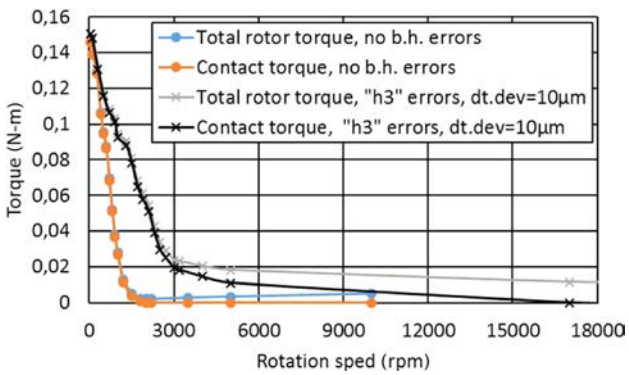

Fig. 18 Torque of the bearing without errors and with h3 bump height errors ($\sigma_{hb} = 10\ \mu$m, $C_r = 31.8\ \mu$m, $W_x = 30$ N, $f = 0.25$)

Figures 18 and 19 show the torque and the power loss calculated for h3 bump heights errors distribution with a standard deviation $\sigma_{hb} = 10\ \mu$m (i.e., 2% of h_b) and for a design radial clearance $C_r = 31.8\ \mu$m. It can be seen that the torque and the power loss variations for bump height errors have different variations compared to the error free bearing. In the case with bump height errors, the contact torque becomes null for a lift-off speed of 17 krpm, i.e., eight times higher than the value of 2 krpm calculated for the error free case.

Figure 20(a) compares the contact power losses obtained for the error distribution h3 but with two values of the standard deviation, 10 μm and 20 μm. It can be seen that for $\sigma_{hb} = 20\ \mu$m there is a permanent contact between the rotor and the top foil; the lift-off speed can, therefore, not be identified.

Results obtained with h4 error distribution are depicted in Fig. 20(b). This distribution has a static stiffness lower than the distribution h3. The contact power losses for h4 have similar maximum values. A lift-off speed can be identified in all cases. Its value is 2 krpm for the error-free case, 3.5 krpm and 10 krpm for

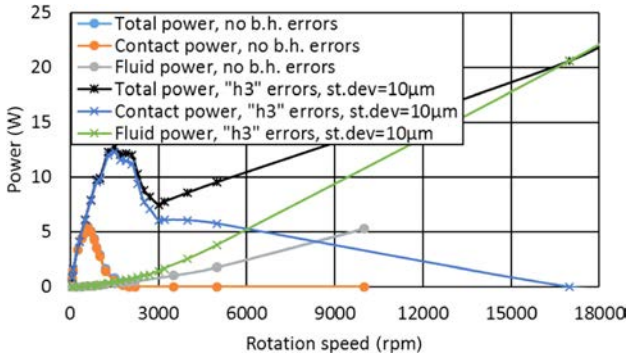

Fig. 19 Comparison of the power loss for the bearing without errors and with h3 bump height errors ($\sigma_{hb} = 10\ \mu$m, $C_r = 31.8\ \mu$m, $W_x = 30$ N, $f = 0.25$)

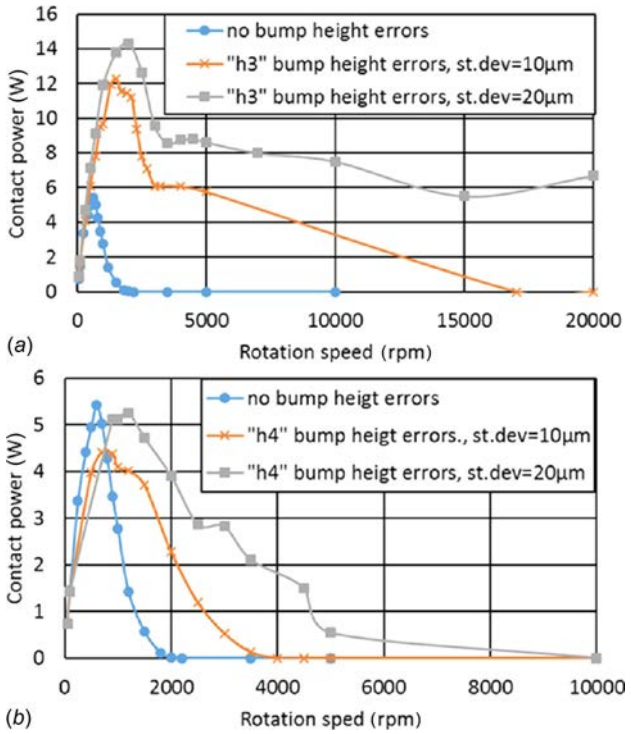

Fig. 20 Comparison of the contact power loss for the bearing without errors and with h3 (*a*) and h4 (*b*) bump height errors ($\sigma_{hb} = 10\ \mu$m and 20 μm, $C_r = 31.8\ \mu$m, $W_x = 30$ N, $f = 0.25$)

the cases with $\sigma_{hb} = 10\ \mu$m and 20 μm, respectively. These results show that a foil bearing with a softer foil structure has better lift-off characteristics than a stiffer foil structure.

These numerical results show the importance of considering the manufacturing errors of the foils when calculating the start-up and lift-off characteristics of these bearings. They also explain the quite different results reported in the literature for the foil bearing with the characteristics given in Table 1. Nevertheless, these are only trends. The manufacturing errors require a more systematic, statistical analysis for quantitatively describing their impact.

High Speeds and Heavy Load Results. The experimental results of Ruscitto et al. [34] enable verification of the theoretical model for high speeds (30 krpm, 45 krpm, and 55.5 krpm) and high static loads (up to 150 N and 190 N).

Ruscitto et al. used a floating bearing-type test rig. It consisted of a rigid, hollow rotor guided by two ball bearings and entrained by an air turbine. The foil bearing was floating mounted between

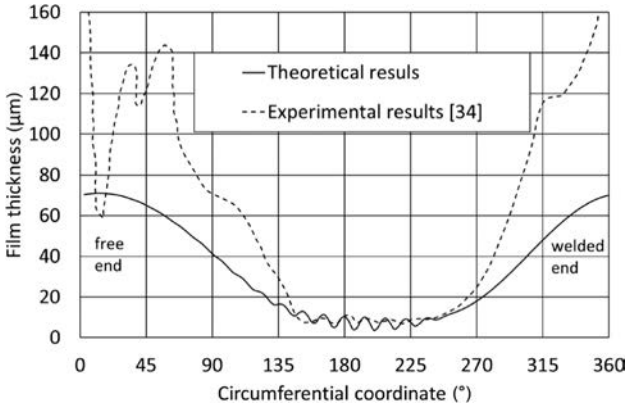

Fig. 21 Circumferential variation of the film thickness ($\Omega =$ 30 krpm, $C_r = 31.8\ \mu$m, $W_x = 134$ N)

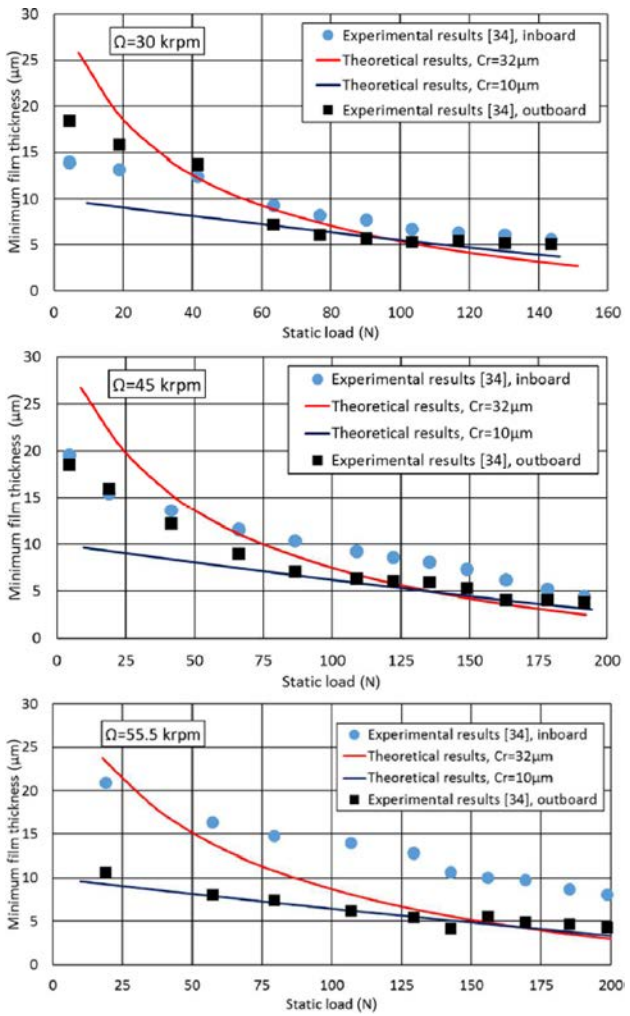

Fig. 22 Minimum film thickness versus static load for three rotation speeds (30 krpm, 45 krpm, and 55 krpm)

the two bearings. The static load was applied directly on the casing of the floating foil bearing. Two inductive proximity probes measured the relative displacements of the foil bearing relative to the rotor. An additional proximity probe was mounted in the hollow rotor and was used together with a slip ring for measuring the air film thickness. Different foil bearing were tested. One of the bearings had exactly the geometrical characteristics given in

Table 1, another bearing had a radial clearance of 57 μm, and other two bearings had an $L/D = 0.5$ with $C_r = 31.8\,\mu$m and 57 μm. Ruscitto et al. measured the radial clearance from static loading measurements. As explained previously, the radial clearance is assimilated with the measured dead-band clearance.

In this work, calculations were made only for the bearing with $L/D = 1$. Figure 21 depicts the circumferential variation of the film thickness for $\Omega = 30$ krpm, $C_r = 31.8\,\mu$m, $W_x = 134$ N. The theoretical results compare very well with Ruscitto's measurements (Fig. VII-20 of Ref. [34]) in the zone of minimum film thickness.

Figure 22 depicts the minimum film thickness for different static loads and three rotation speeds (30 krpm, 45 krpm, and 55.5 krpm). Ruscitto's measurements were performed both in the mid-plane and in the end-plane of the bearing. The present calculations were performed with the 31.8 μm radial clearance reported by Ruscitto et al. and with the 10 μm radial clearance used in Ref. [13] for the same comparisons. The calculated results make no distinction between the film thickness at the bearing mid and end planes because the structural model is two-dimensional and uses the axially averaged pressures to calculate the load applied on the top foil. Thus, the theoretical film thickness has an axially constant value.

Figure 22 shows the impact of the radial clearance on the axially averaged minimum film thickness. For low and moderate loads, the values calculated with $C_r = 10$ μm are lower while for high static loads the value of the radial clearance had a negligible impact. Also for high loads, the calculated results slightly underestimate the measured minimum film thickness. The differences increase with increasing rotation speed but this can be due to different causes. Indeed, it was repeatedly reported in the literature that the foil bearing with $L/D = 1$ shows at least $\Omega/2$ subsynchronous if not unstable vibrations when the rotation speed approaches 30 krpm. This threshold is increased with increasing the static load but it is probable that vibrations, at least of synchronous origin, affected the results of very high speed tests. By the way, Ruscitto et al. always report in Ref. [34] a dynamic shaft orbit that increases with the rotation speed from 5 μm to 13 μm.

Figure 23 depicts the attitude angle versus the static load. The values calculated with a radial clearance of 10 μm show a very light variation with the static load, especially for the highest rotation speed.

This is not the case for the results obtained with $C_r = 31.8\,\mu$m that decreased clearly with the static load. For $\Omega = 30$ krpm and 45 krpm, the values measured by Ruscitto et al. lie between the theoretical results while for $\Omega = 55.5$ krpm, they are closer to the values calculated with $C_r = 31.8\,\mu$m.

All the theoretical results show a reasonable agreement with measurements. It must be underlined that these tests represent difficult operating conditions for a foil bearing of this size because the static loads are extremely large. Moreover, the minimum film thickness of a foil bearing is very difficult to measure due to its compliance. The values reported by Ruscitto et al. are very low, sometimes lower than 5 μm. One should have in mind that the upper limit of the mixed lubrication regime for this bearing was considered to be close to $3\sigma_{eq} = 2.1\,\mu$m so very close to the values depicted in Fig. 22.

It should be also underlined that the largest differences between the calculated and the measured results appear at lower static loads. The differences for large values of the static loads are systematic smaller. This is due to the simplified 2D model of the foil structure loaded by axially averaged pressures. The model is close to reality for high static loads when the film thickness is very small and the axial pressure field is almost flat. For low and mild static loads, the axial pressure field is parabolic and the approximation of an axially averaged pressure deforming the foil structure can be questioned. However, the assumption of an axially averaged pressure is coherent with the 2D model of the foil structure. It is the price for obtaining a theoretical model that necessitates less computational time than a full nonlinear finite element approach as used in Ref. [24].

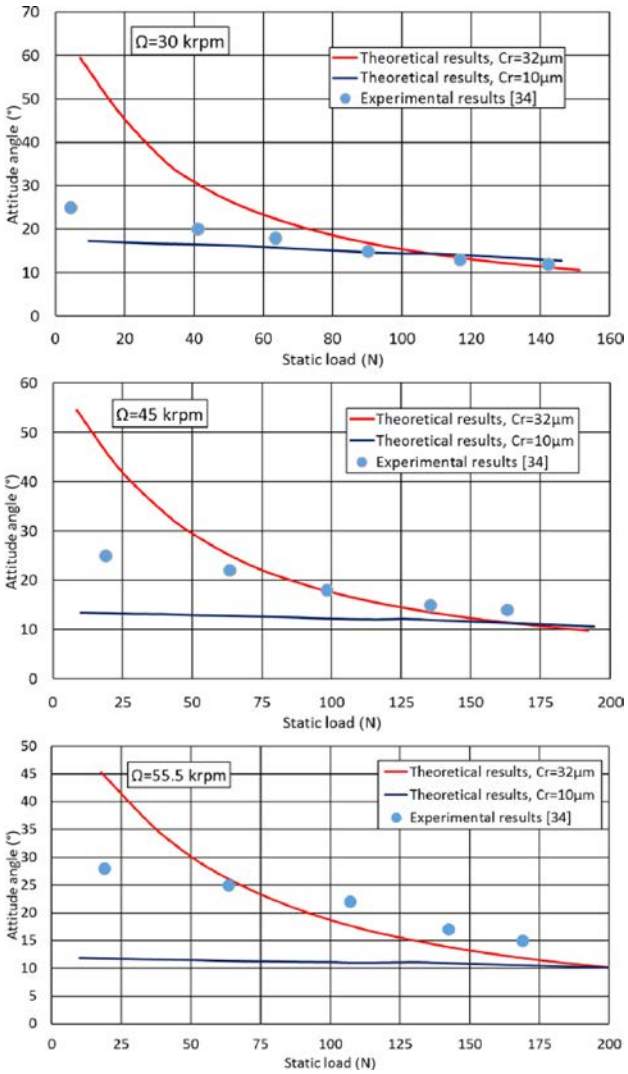

Fig. 23 Attitude angle versus static load for three rotation speeds (30 krpm, 45 krpm, and 55 krpm)

Summary and Conclusions

The model presented in this work is able to deal with all operating conditions of aerodynamic foil bearings, from start-up to high speed and high static loadings. This ability comes from modeling the foils and the rotor as a structure with close-loose gaps. Contact algorithms are then able to solve the noninterference conditions. Considering the local radial clearance as a gap submitted to Signorini–Moreau contact conditions avoids any interference between the rotor and the top foil. The rotor/top foil gap is always a positive distance. If this gap is less than $3\sigma_{eq}$ (i.e., three times the standard deviation of the combined roughness of the rotor and top foil), then the thin film flow is dealt with as a mixed lubrication problem. This enabled the calculation of the start-up torque that compared very well with experimental data.

Another advantage of describing the foils as a structure with gaps is the possibility of modeling manufacturing errors. The ambiguous concept of radial clearance of foil bearings can thus be explained. Results obtained for the takeoff speed show that the manufacturing errors lead to its increase and may even disable the development of a complete air film.

Results obtained for high rotation speeds and high static loads proved the capability of the foil bearing model to deal with all operating conditions.

Funding Data

- Centre National d'Etudes Spatiales (CNES) (Funder ID: 10.13039/501100002830).
- Airbus Safran Launchers (Funder ID: 10.13039/501100003204).

Nomenclature

C_r = design radial clearance, m
e = foil thickness, m
E = Young modulus of elasticity, Pa
f = friction coefficient
$F, \boldsymbol{F}$ = force and force vector, N
$\mathcal{F}$ = Gaussian probability distribution
g = gap, m
h = film thickness, m
$\bar{h}$ = dimensionless film thickness, $\bar{h} = h/\sigma_{\text{eq}}$
h_b = bump height, m
$\boldsymbol{K}$ = stiffness matrix, N/m
$k_1,\ldots, k_4$ = stiffness of the truss model, N/m
L = bearing length, m
$\boldsymbol{L}$ = matrix, N/m
l_0 = bump half width, m
n = number of iterations in Eqs. (7) and (29)
N = number of contacts
nb = number of bumps of the corrugated foil
nx = number of circumferential discretization points
$P, \tilde{P}$ = pressure, Pa
p_b = bump pitch, m
r = distance between the rotor and the undeformed top foil, m
R = bearing radius, m
$\mathfrak{r}_{h\text{film}}$ = relaxation coefficient in Eq. (29)
$\boldsymbol{S}$ or s_{ij} = elasticity matrix of the top foil, m/N
$u, \boldsymbol{u}$ = displacement and displacement vector, m
$W_{x,y}$ = static load, N
x, y = Cartesian coordinates
X, Y = axes of the Cartesian coordinates system
y_s = parameters of the Gaussian probability distribution
β = roughness radius, m
ε = penalty parameter, N/m
η = roughness surface density, m^{-2}
θ = angular coordinate, rad
$\bar{\lambda}$ = augmented Lagrange multiplier, N
μ = dynamic viscosity, Pa·s
ν = Poisson coefficient
Π = potential energy, j
σ = standard deviation, m
Ω = rotation speed, rad/s

Subscripts

ALM = augmented Lagrange multiplier
avrg = average
b = bottom
cntct = contact
eq = equivalent
ext = external ambient
f = friction
i, j = bump number
n = normal
p = pressure
R = rotor
t = top foil
0 = initial value

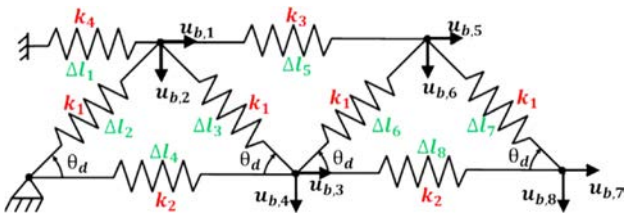

Fig. 24 The elastic model of the bump foil

Appendix A

The Structural Model of the Bump Foil. The bumps of the corrugated foil are modeled as an unwrapped structure of interacting springs. Figure 24 depicts this model for a foil with two bumps. The model is two-dimensional because the elasticity in the axial direction is not considered. Each bump has four DOF and the stiffness of springs is deduced by using Castigliano's relations. The procedure was detailed in Ref. [25] for bumps with three DOF ($u_{b,4}$ and $u_{b,8}$ were not considered) and was extended in Ref. [31] for four DOF.

The stiffness of the corrugated foil is written by superposing individual bump stiffness and coupling matrices. For example for a corrugated foil with two bumps, this yields

$$\boldsymbol{K}_{2\boldsymbol{b}} = \begin{bmatrix} \boldsymbol{K}_4 + \boldsymbol{K}_{\boldsymbol{b}} + \boldsymbol{K}_3 & \boldsymbol{K}_{\boldsymbol{c}}^T \\ \boldsymbol{K}_{\boldsymbol{c}} & \boldsymbol{K}_{\boldsymbol{b}} + \boldsymbol{K}_3 \end{bmatrix} \tag{A1}$$

$$\boldsymbol{K}_{\boldsymbol{b}} = \begin{bmatrix} 2k_1c^2 & 0 & -k_1c^2 & -k_1sc \\ 0 & 2k_1s^2 & -k_1sc & -k_1s^2 \\ -k_1c^2 & -k_1sc & k_2 + k_1c^2 & k_1cs \\ -k_1sc & -k_1s^2 & k_1cs & k_1s^2 \end{bmatrix} \tag{A2}$$

$$\boldsymbol{K}_{\boldsymbol{b}} = \begin{bmatrix} -k_3 & 0 & -k_1c^2 & k_1cs \\ 0 & 0 & k_1cs & -k_1s^2 \\ 0 & 0 & -k_2 & 0 \\ 0 & 0 & 0 & 0 \end{bmatrix} \tag{A3}$$

$$\boldsymbol{K}_{3/4} = \begin{bmatrix} k_{3/4} & 0 & 0 & 0 \\ 0 & 0 & 0 & 0 \\ 0 & 0 & 0 & 0 \\ 0 & 0 & 0 & 0 \end{bmatrix} \tag{A4}$$

The extension of Eq. (A1) to an arbitrary number of bump is immediate.

Appendix B

The Structural Model of the Top Foil. The top foil is modeled by using a circular (curved) beam with the plate correction. The variation of its elastic characteristics in the axial direction is discarded. The elasticity matrix of the top foil is obtained with Bresse relations

$$\bar{s}_{i,j} = \begin{cases} \dfrac{\cos\theta_i \sin\theta_j}{2} - \dfrac{\theta_j \cos(\theta_i - \theta_j)}{2}, \text{ if } \theta_j \le \theta_i \\ \dfrac{\cos\theta_j \sin\theta_i}{2} - \dfrac{\theta_i \cos(\theta_j - \theta_i)}{2}, \text{ otherwise} \end{cases} \tag{B1}$$

$$s_{i,j} = \frac{R^3}{Le^3/12} \frac{1-\nu^2}{E} \bar{s}_{i,j}, \theta_i, \theta_j > 0,\ i,j = 1\ldots nb \cup nx \tag{B2}$$

where the angle θ is measured from the welding (Fig. 1) in clockwise direction. The stiffness matrix of the top foil is $\boldsymbol{K}_{\boldsymbol{t}} = \boldsymbol{S}^{-1}$.

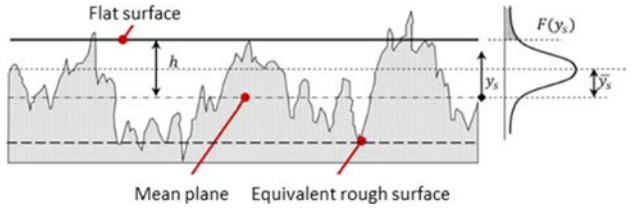

Fig. 25 The equivalent rough surface

Appendix C

The Greenwood and Williamson Contact Model. The model considers the contact between a virtual flat, rigid surface, and an elastic surface carrying the cumulated roughness of the rotor and of the top foil (Fig. 25).

The equivalent elasticity modulus of this surface is

$$E_{\text{eq}} = \left(\frac{1-\nu_R{}^2}{E_R} + \frac{1-\nu_t{}^2}{E_t} \right)^{-1} \tag{C1}$$

The local film thickness is the distance between the virtual flat surface and the average plane of the surface carrying the cumulated roughness. The height of the asperities measured from the average plane is y_s. Asperities with a height larger than the local film thickness will be in contact with the virtual flat surface and will generate contact forces. The asperities are supposed to be spheres of the same radius β. Following Hertz theory, the contact force for a single asperity

$$F_{\text{Hrtz}} = \frac{4}{3} E_{\acute{e}\text{q}} \sqrt{\beta} (y_s - h)^{3/2} \tag{C2}$$

The total number of roughness on a discretization cell of the Reynolds is

$$N_{\text{asp}} = (\eta_R + \eta_t)\mathcal{A} \tag{C3}$$

Greenwood and Williamson suppose that the roughness height follows a Gaussian probability distribution, $\mathcal{F}$. In this case, the force from all contact asperities in a discretization cell is

$$\begin{aligned} F_{\text{asp}} &= N_{\text{asp}} \int_h^\infty F_{\text{Hrtz}} \mathcal{F}(y_s) dy_s \\ &= \frac{4}{3} N_{\text{asp}} E_{\text{eq}} \sqrt{\beta} \int_h^\infty (y_s - h)^{3/2} \mathcal{F}(y_s) dy_s \end{aligned} \tag{C4}$$

A good approximation of the Gaussian probability distribution is:

$$\begin{aligned} &\mathcal{F}(y_s) = \frac{35}{32c^7} \left(c^2 - y_s^2\right)^3, \text{ if } -c \le y_s \le c \\ &\mathcal{F}(y_s) = 0 \text{ otherwise} \end{aligned} \tag{C5}$$

where $c = 3\sigma_{\text{eq}}$. The integral in Eq. (C4) can then be analytically calculated.

The characteristics of the contact surfaces used in this work are given in Table 2.

Table 2 Parameters of the rough contact surfaces

η_R (m^{-2})	4×10^9	η_t (m^{-2})	4×10^9
σ_R (μm)	0.5	σ_t (m)	0.5
E_R (GPa)	200	E_t (GPa)	200
ν_R	0.29	ν_t	0.29
β (μm)	0.52		

References

[1] Heshmat, H., Walowit, J. A., and Pinkus, O., 1983, "Analysis of Gas-Lubricated Foil Journal Bearings," ASME J. Lubr. Technol., **105**(4), pp. 647–655.

[2] Branagan, M., Griffin, D., Goyne, C., and Untaroiu, A., 2015, "Compliant Gas Foil Bearings and Analysis Tools," ASME J. Eng. Gas Turbines Power, **138**(5), p. 054001.

[3] Iordanoff, I., 1999, "Analysis of an Aerodynamic Compliant Foil Thrust Bearing: Method for a Rapid Design," ASME J. Tribol., **121**(4), pp. 816–822.

[4] Peng, J. P., and Carpino, M., 1993, "Calculation of Stiffness and Damping Coefficients for Elastically Supported Gas Foil Bearings," ASME J. Tribol., **115**(1), pp. 20–27.

[5] Rubio, D., and San Andres, L., 2007, "Structural Stiffness, Dry Friction Coefficient, and Equivalent Viscous Damping in a Bump-Type Foil Gas Bearing," ASME J. Eng. Gas Turbines Power, **129**(2), pp. 494–502.

[6] Kim, T. H., and San Andreś, L., 2009, "Effect of Side Feed Pressurization on the Dynamic Performance of Gas Foil Bearings: A Model Anchored to Test Data," ASME J. Eng. Gas Turbines Power, **131**(1), p. 012501.

[7] Ryu, K., 2012, "Prediction of Axial and Circumferential Flow Conditions in a High Temperature Foil Bearing With Axial Cooling Flow," ASME J. Eng. Gas Turbines Power, **134**(9), p. 094503.

[8] Bonello, P., and Pham, H. M., 2014, "The Efficient Computation of the Nonlinear Dynamic Response of a Foil-Air Bearing Rotor System," J. Sound Vib., **333**(15), pp. 3459–3478.

[9] Carpino, M., Medvetz, L. A., and Peng, J. P., 1994, "Effects of Membrane Stresses in the Prediction of Foil Bearing Performance," Tribol. Trans., **37**(1), pp. 43–50.

[10] Peng, J. P., and Carpino, M., 1997, "Finite Element Approach to the Prediction of Foil Bearing Rotor Dynamic Coefficients," ASME J. Tribol., **119**(1), pp. 85–90.

[11] Carpino, M., and Talmage, G. A., 2003, "Fully Coupled Finite Element Formulation for Elastically Supported Foil Journal Bearings," Tribol. Trans., **46**(4), pp. 560–565.

[12] Bruckner, R. J., 2004, "Simulation and Modeling of the Hydrodynamic, Thermal and Structural Behavior of Foil Thrust Bearings," Doctoral dissertation, Case Western Reserve University, Cleveland, OH.

[13] San Andrés, L., and Kim, T. H., 2009, "Analysis of Gas Foil Bearings Integrating FE Top Foil Models," Tribol. Int., **42**(1), pp. 111–120.

[14] Kim, D., and Park, S., 2009, "Hydrostatic Air Foil Bearings: Analytical and Experimental Investigations," Tribol. Int., **42**(3), pp. 413–425.

[15] Leister, T., Baum, C., and Seemann, W., 2017, "Computational Analysis of Foil Air Journal Bearings Using a Runtime-Efficient Segmented Foil Model," ASME J. Fluids Eng., **140**(2), p. 021115.

[16] Lee, D.-H., Kim, Y.-C., and Kim, K. W., 2008, "The Static Performance Analysis of Foil Journal Bearings Considering Three-Dimensional Shape of the Foil Structure," ASME J. Tribol., **130**(3), p. 031102.

[17] Lee, D. H., Kim, Y. C., and Kim, K. W., 2010, "The Effect of Coulomb Friction on the Static Performance of Foil Journal Bearings," Tribol. Int., **43**(5–6), pp. 1065–1072.

[18] Lehn, A., Mahner, M., and Schweizer, B., 2016, "Elasto-Gasdynamic Modeling of Air Foil Thrust Bearings With a Two-Dimensional Shell Model for Top and Bump Foil," Tribol. Int., **100**, pp. 48–59.

[19] Barzem, L., Bou-Said, B., Rocchi, J., and Grau, G., 2013, "Aero-Elastic Bearing Effects on Rotor Dynamics: A Numerical Analysis," Lubr. Sci., **25**(7), pp. 463–478.

[20] Larsen, J. S., Varela, A. C., and Santos, I. F., 2014, "Numerical and Experimental Investigation of Bump Foil Mechanical Behavior," Tribol. Int., **74**, pp. 46–56.

[21] Zywica, G., 2011, "The Static Performance Analysis of the Foil Bearing Structure," Acta Mech. Autom., **5**(4), pp. 119–122.

[22] Temis, Y. M., Temis, M. Y., and Meshcheryakov, A. B., 2011, "Gas-Dynamics Foil Bearing Model," J. Frict. Wear, **32**(3), pp. 212–220.

[23] Liu, J., and Du, F., 2012, "Simulation of Compliant Bump Foil Journal Bearing Using Coupled Reynolds Equation and Finite Element Model Method," Adv. Mater. Res., **479–481**, pp. 2499–2503.

[24] Fatu, A., and Arghir, M., 2017, "Numerical Analysis of the Impact of Manufacturing Errors on the Structural Stiffness of Foil Bearings," ASME J. Eng. Gas Turbines Power, **140**(4), p. 041506.

[25] Le Lez, S., Arghir, M., and Frene, J., 2007, "A New Bump-Type Foil Bearing Structure Analytical Model," ASME J. Eng. Gas Turbines Power, **129**(4), pp. 1047–1057.

[26] Hryniewicz, P., Wodtke, M., Olszewski, A., and Rzadkowski, R., 2009, "Structural Properties of Foil Bearings: A Closed Form Solution Validated With Finite Element Analysis," Tribol. Trans., **52**(4), pp. 435–446.

[27] Feng, K., and Kaneko, S., 2010, "Analytical Model of Bump-Type Foil Bearings Using a Link-Spring Structure and a Finite Element Shell Model," ASME J. Tribol., **132**(2), p. 021706.

[28] Gad, A. M., and Kaneko, S., 2014, "A New Structural Stiffness Model for Bump-Type Foil Bearings: Application to Generation II Gas Lubricated Foil Thrust Bearing," ASME J. Tribol., **136**(4), p. 041701.

[29] Von Osmanski, S., Larsen, J. S., and Santos, I. F., 2017, "A Fully Coupled Air Foil Bearing Model Considering Friction—Theory & Experiment," J. Sound Vib., **400**, pp. 660–679.

[30] Hoffmann, R., Munz, O., Pronobis, T., Barth, E., and Liebich, R., 2018, "A Valid Method of Gas Foil Bearing Parameter Estimation: A Model Anchored on Experimental Data," J. Mech. Eng. Sci., **232**(24), pp. 4510–4527.

[31] Arghir, M., and Benchekroun, O., 2019, "A Simplified Structural Model of Bump-Type Foil Bearings Based on Contact Mechanics Including Gaps and Friction," Tribol. Int., **134**, pp. 129–144.
[32] Wriggers, P., and Zavarise, G., 2006, *Computational Contact Mechanics*, 2nd ed., Vol. 518, Springer-Verlag, Berlin, pp. 195–226.
[33] Rudloff, L., Arghir, M., Bonneau, O., and Matta, P., 2011, "Experimental Analyses of a First Generation Foil Bearing. Start-Up Torque and Dynamic Coefficients," ASME J. Eng. Gas Turbines Power, **133**(9), p. 092501.
[34] Ruscitto, D., Mc Cormick, J., and Gray, S., 1978, "Hydrodynamic Air Lubricated Compliant Surface Bearing for an Automotive Gas Turbine Engine I-Journal Bearing Performance," NASA, Lewis Research Center, Cleveland, OH, Report No. NASA CR-135368.
[35] Arghir, M., Lez, S. L., and Frene, J., 2006, "Finite Volume Solution of the Compressible Reynolds Equation—Linear and Non Linear Analysis of Gas Bearings," Proc. Inst. Mech. Eng., Part J, **220**(7), pp. 617–627.
[36] Patir, N., and Cheng, H. S., 1979, "Application of Average Flow Model to Lubrication Between Rough Sliding Surfaces," ASME J. Lubr. Technol., **101**(2), pp. 220–229.
[37] Greenwood, J. A., and Williamson, J. B. P., 1966, "Contact of Nominally Flat Surfaces," Proc. R. Soc. London A, **295**(1442), pp. 300–319.
[38] Le Lez, S., 2007, "Caractéristiques Statiques et Dynamiques des Paliers à Feuilles," thèse de doctorat, Université de Poitiers, Poitiers, France.